

Large magneto-optical effect and magnetic anisotropy energy in two-dimensional ferromagnetic metal Fe_3GeTe_2

Ming-Chun Jiang¹ and Guang-Yu Guo^{1,2,*}

¹*Department of Physics and Center for Theoretical Physics, National Taiwan University, Taipei 10617, Taiwan*

²*Physics Division, National Center for Theoretical Sciences, Hsinchu 30013, Taiwan*

(Dated: June 24, 2022)

Few layers Fe_3GeTe_2 is currently the only atomically thin ferromagnetic metal, and thus has drawn huge attention in the field of two-dimensional (2D) magnetism. In this paper, we perform a systematic first principle study on the electronic structure, magnetic anisotropy energy (MAE), and magneto-optical (MO) effects in monolayer (ML), bilayer (BL) and trilayer (TL) as well as bulk Fe_3GeTe_2 . All the considered structures of Fe_3GeTe_2 are predicted to have large MAE of order ~ 3.0 meV/f.u., being larger than reported 2D ferromagnetic semiconductors $\text{Cr}_2\text{Ge}_2\text{Te}_6$ and CrI_3 and also being comparable to that of FePt which has the largest MAE among the transition metal alloys. This large MAE thus stabilizes the long range ferromagnetic order down to atomically thin layers and also suggests promising applications of 2D Fe_3GeTe_2 in high density data storage. Furthermore, the calculated magneto-optical spectra show large magnetic circular dichroism, thus resulting in large MO Kerr rotation and Faraday rotation angles. In visible frequency range, huge Kerr rotation angles up to $\sim 2.7^\circ$ for TL Fe_3GeTe_2 are found. Such values are larger than famous MO transition metal alloy MnBi . Also, large Faraday rotation angles are predicted for all considered Fe_3GeTe_2 structures. In particular, ML Fe_3GeTe_2 has a Faraday rotation angle of $-156^\circ/\mu\text{m}$, which is three times larger than famous MO oxide $\text{Bi}_3\text{Fe}_5\text{O}_{12}$. These important findings are analysed in terms of the calculated orbital-decomposed density of states and dipole selection rule derived from the group theory. Our findings thus suggest that few layers and bulk Fe_3GeTe_2 are promising MO materials and could be widely applied to nano MO devices in the future.

I. INTRODUCTION

Ever since the discovery of intrinsic magnetism in atomically thin films of semiconductors CrI_3 and $\text{Cr}_2\text{Ge}_2\text{Te}_6$ [1, 2] as well as metal Fe_3GeTe_2 [3], the field of two-dimensional (2D) magnetism is subjected to intensive studies. The significance of 2D magnetism stems from the famous Mermin-Wagner theorem [4], which predicts that thermal fluctuation prohibits any long range order in isotropic 2D systems at any finite temperature. 2D magnetic materials are desired for applications such as magnetic memories, magnetic sensing and magneto-optical (MO) devices. Remarkably, few layers Fe_3GeTe_2 are currently the only ferromagnetic metals that retain their magnetism till atomically thin layers [5, 6]. Thus bulk and few layers Fe_3GeTe_2 have been studied intensively.

Bulk Fe_3GeTe_2 was discovered to have high Curie temperature of ~ 220 K [7, 8] and a high spin-orbit torque switching efficiency of 1.66 in $\text{Fe}_3\text{GeTe}_2/\text{Pt}$ heterostructure [9]. Also, large anomalous Hall conductivity of up to 550 S/cm [10–13] and large anomalous Nernst conductivity of -0.217 A/m-K [13, 14] has been reported. Interestingly, a large suppression of magnetic anisotropy of nearly 33% through 0.5 hole doping has been predicted for bulk Fe_3GeTe_2 [19].

Excitingly, the intrinsic magnetism in few layers Fe_3GeTe_2 has been discovered very recently through re-

fractive magnetic circular dichroism (RMCD) experiments [3, 15]. Furthermore, owing to its metallic nature, a gate-tunable Curie temperature from ~ 100 K to ~ 300 K in trilayer Fe_3GeTe_2 has been reported [3]. As for the spin-transport properties, a pressure- and layer-dependent anomalous Hall conductivity has been predicted [12, 16]. Large magnetic anisotropy energy (MAE) of ~ 2.0 meV/f.u. was measured [3] and its tunability via electric gating were also predicted [17, 18]. Fe_3GeTe_2 thus show rich physics phenomenon and feasible applications to future technology. Thus, the mechanism behind the physical properties of this atomically thin ferromagnetic metal should be fully investigated.

In this paper, we carry out a systematic first principles density functional theory study on the magnetic, electronic, optical and magneto-optical properties of monolayer (ML), bilayer (BL) and trilayer (TL) as well as bulk Fe_3GeTe_2 . In particular, we focus on the magnetic anisotropy energy (MAE) and the MO effects in these structures. Also, we try to correlate the MAE and MO effects with the calculated electronic structures to have a better picture of their possible origins. Although the MAE of ML Fe_3GeTe_2 has been studied both experimentally and theoretically [17–19], the MAE of BL and TL Fe_3GeTe_2 has not been reported yet. Furthermore, there has been no theoretical study on the optical and MO effects in Fe_3GeTe_2 .

Magnetic anisotropy energy depicts the energy needed to rotate the magnetization direction from the easy axis to the hard axis. MAE plays a crucial role in suppressing thermal fluctuation and thus stabilizes long-range magnetic orders in 2D systems. It is also an important fac-

* gyguo@phys.ntu.edu.tw

tor that characterizes a magnetic material. In particular, a thin film with a large perpendicular magnetic anisotropy may find applications in high density magnetic data storage. It consists of the magnetocrystalline anisotropy energy (C-MAE) and the magnetic dipolar anisotropy energy (D-MAE). C-MAE is due to difference between the relativistic band structures for two different magnetic orientations. On the other hand, D-MAE originates from the classical magnetic dipole-dipole interaction in the magnetic solid [20, 21]. Interestingly, D-MAE is determined solely by the geometric shape of the atomic and magnetic structure [20, 21]. In layered materials, the D-MAE always prefers an in-plane magnetization while C-MAE could favor either an in-plane or the out-of-plane magnetization[22]. So far only the effect of the chemical doping on the MAE in bulk Fe_3GeTe_2 and the gating effect on the MAE of ML Fe_3GeTe_2 have been investigated. Therefore, in this paper, we present both calculated C-MAE and D-MAE in 2D and bulk Fe_3GeTe_2 to investigate the thickness-dependence of the MAE.

Magneto-optical effects are manifestations of the interplay between magnetism and light in magnetic solids [23, 24]. When a linearly polarized light beam hits a magnetic material, the principal axis of the reflected and transmitted light rotates with respect to the polarization direction of the incident light. The former is called the magneto-optical Kerr effect (MOKE) and the latter is known as the magneto-optical Faraday effect (MOFE). MO effects originate the simultaneous presence of the relativistic spin-orbit coupling (SOC) and spontaneous magnetization in the magnetic solid. The spontaneous magnetization and the SOC result in energy band splitting and thus lead to different refractive indexes for the right- and left-circularly light. MOKE has been widely applied to study the magnetic properties of thin films and surfaces [24]. In the case of Fe_3GeTe_2 and other 2D ferromagnets, long range magnetic orders were indeed discovered by the MOKE or RMCD experiments [1-3, 15]. Large MOKE and MOFE effects can also be exploited for prominent high density MO data storage and MO sensors. [27, 28] The emergence of 2D magnetic materials could lead these applications to an even smaller length scale.

It is well-known that 3d transition metals and alloys are famous MO materials with bcc Fe having a significant Kerr rotation angle of $\sim 0.5^\circ$. [24] Also, 3d transition alloys that contain heavy elements such as FePt were discovered to have large MO effects due to the large SOC strength in the heavy element atoms [29, 30]. In the present case, firstly, Fe_3GeTe_2 has partially filled Fe 3d orbitals [18, 19]. Secondly, Te is a heavy element, which introduces strong SOC. On top of that, previously studied 2D magnetic materials $\text{Cr}_2\text{Ge}_2\text{Te}_6$ [22] and CrI_3 [31] were reported to have significant MOKE and MOFE. Hence, MO effects on 2D magnetic materials could be promising. Therefore, 2D and bulk Fe_3GeTe_2 are expected to have large MO effects. Therefore, we perform a systematic *ab initio* density functional study of the op-

tical and MO properties of bulk and 2D Fe_3GeTe_2 . As will be shown in Sec. III C and D, we indeed find a large MOKE angle of $\sim 2.7^\circ$ for thin films Fe_3GeTe_2 . Furthermore, we also find a large MOFE angle of $\sim 156^\circ/\mu\text{m}$. These all suggest that bulk and ultrathin films Fe_3GeTe_2 are promising MO materials for technological applications.

II. STRUCTURES AND METHODS

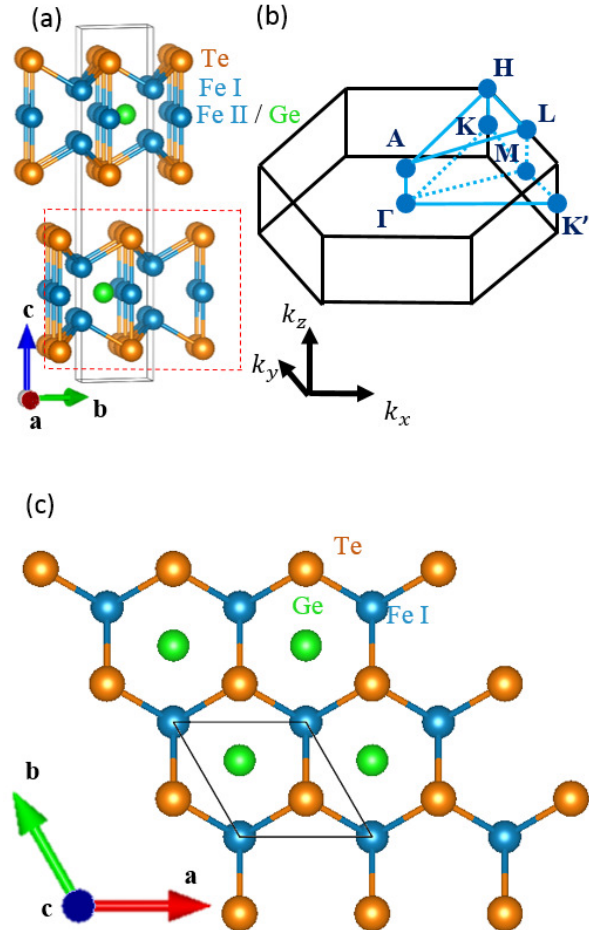


FIG. 1. (a) Side view of layered hexagonal structure of Fe_3GeTe_2 unit cell with two formula units within. The red dashed rectangle indicates one monolayer. Note that there are two inequivalent Fe sites. (b) The corresponding Brillouin zone. The 2D Brillouin zone would be the Γ -K-M plane. (c) Top view of monolayer Fe_3GeTe_2 with ABA-stacked triangular lattice layers.

Bulk Fe_3GeTe_2 forms a layered hexagonal structure with van der Waals (vdW) gap in between two monolayers. Each Fe_3GeTe_2 ML is consisted of five triangular lattice plane where two Te planes sandwich three ABA-stacked Fe planes. In the middle plane (FeII/Ge)(Fig. 1(a)), one Ge atom is located right in the center of the

Fe triangle and the two sites (FeII and Ge in Fig. 1(a)) interchanges between each ML. Thus, bulk Fe_3GeTe_2 possesses a $P6_3/mmc$ symmetry with two formula units(f.u.) per unit cell(Fig. 1(a)) [7]. The experimental lattice constants are $a = 3.991 \text{ \AA}$ and $c = 16.33 \text{ \AA}$ [7]. Due to lack of experimental structure on few-layer Fe_3GeTe_2 , we have optimized the lattice constants and atomic positions for bulk and few-layer Fe_3GeTe_2 for consistency. The few-layer structures are modelled utilizing slab-superlattice approach with the separations between MLs being 16 \AA .

Ab initio calculations are performed using the accurate projector-augmented wave (PAW) method [32] implemented in the Vienna *ab initio* simulation package (VASP) [33, 34]. The exchange-correlation interaction is treated with the generalized gradient approximation (GGA) parametrized by the Perdew-Burke-Ernzerhof (PBE) formula [35]. The valence electron configurations of Fe, Ge, Te taken into account are $3p^6 3d^7 4s^1$, $3d^{10} 4s^2 4p^2$, $5s^2 5p^4$, respectively. A large plane wave cut-off energy of 400 eV is used. For the Brillouin zone integrations, Γ - centered k -meshes of $16 \times 16 \times 4$ and $16 \times 16 \times 1$ with the tetrahedron method [36] are used for bulk and few-layer Fe_3GeTe_2 , respectively. On account of the need of a fully structural optimization for both bulk and few-layers Fe_3GeTe_2 , we have added the DFT-D2 vdW correction methods of Grimme [37] implemented in VASP inside the calculation in combination with the PBE functional. The bulk theoretical lattice constants agree well with experimental data [7] ($a = 3.995 \text{ \AA}$ (0.1 % error), $c = 16.73 \text{ \AA}$ (0.35 % error)). Using the same method, the optimized lattice constant a we obtained for 1-3 layers Fe_3GeTe_2 is 4.01 \AA .

MAE consists of C-MAE and D-MAE. For C-MAE, we first perform two relativistic calculations for the in-plane magnetization and the out-of-plane magnetization. Then the energy difference between these two calculations would be the C-MAE ($\Delta E_c = E^{[100]} - E^{[001]}$). A large energy cut-off of 450 eV with dense k -point meshes of $24 \times 24 \times 6$ is used for bulk Fe_3GeTe_2 and a energy cut-off of 400 eV with dense k -point meshes of $32 \times 32 \times 1$ is used for 1-3 layers Fe_3GeTe_2 to obtain C-MAE that is well-converged within 3 %. As for the D-MAE, for ferromagnetic systems, the D-MAE in atomic Rydberg units is given by [20, 21]

$$E_d = \sum_{qq'} \frac{2m_q m_{q'}}{c^2} M_{qq'} \quad (1)$$

where the speed of light $c = 274.072$ and the so-called magnetic dipolar Madelung constant

$$M_{qq'} = \sum_{\mathbf{R}} \frac{1}{|\mathbf{R} + \mathbf{q} + \mathbf{q}'|^3} \left\{ 1 - 3 \frac{[(\mathbf{R} + \mathbf{q} + \mathbf{q}') \cdot \hat{m}_q]^2}{|\mathbf{R} + \mathbf{q} + \mathbf{q}'|^2} \right\} \quad (2)$$

where \mathbf{R} are the lattice vector, \mathbf{q} are the atomic position vectors in the unit cell, and m_q is the atomic magnetic moment (in units of μ_B) on site \mathbf{q} . Utilizing the

calculated magnetic moments, the ΔE_d is obtained as the difference in E_d between the in-plane and out-of-plane magnetizations. In 2D systems, due to all in-plane \mathbf{R} and \mathbf{q} , an out-of-plane magnetization would result in zero for the second term in Eq.(2). Thus, the $M_{qq'}$ for in-plane magnetization is negative while being positive for out-of-plane magnetization. Therefore, D-MAE always prefers the in-plane magnetization in 2D magnetic systems [22, 31]. This is a purely geometrical effect and consequently D-MAE is also called the magnetic shape anisotropy energy.

For a solid with at least threefold rotational symmetry and a magnetization along rotational z -axis, the non-zero components for the optical conductivity is σ_{xx} , σ_{zz} , and σ_{xy} . We then calculate these three independent elements using the Kubo formula within linear-response theory [38–40]. The absorptive parts of these elements are given by:

$$\sigma_{aa}^1(\omega) = \frac{\pi e^2}{\hbar \omega m^2} \sum_{i,j} \int_{BZ} \frac{d\mathbf{k}}{(2\pi)^3} |p_{ij}^a|^2 \delta(\epsilon_{\mathbf{k}j} - \epsilon_{\mathbf{k}i} - \hbar\omega), \quad (3)$$

$$\sigma_{xy}^2(\omega) = \frac{\pi e^2}{\hbar \omega m^2} \sum_{i,j} \int_{BZ} \frac{d\mathbf{k}}{(2\pi)^3} \text{Im} [p_{ij}^x p_{ij}^y] \delta(\epsilon_{\mathbf{k}j} - \epsilon_{\mathbf{k}i} - \hbar\omega), \quad (4)$$

where $\hbar\omega$ is the photon energy and $\epsilon_{\mathbf{k}i}$ is the i th band energy at point \mathbf{k} . Summations i and j are over the occupied and unoccupied bands, respectively. Dipole matrix elements $p_{ij}^a = \langle \mathbf{k}j | \hat{p}_a | \mathbf{k}i \rangle$, where \hat{p}_a denotes the Cartesian component a of the dipole operator, are obtained from the relativistic band structure within PAW formalism [41]. The integration is over the whole Brillouin zone using the linear tetrahedron method [42]. The dispersive part of the optical conductivity elements can be obtained from its corresponding absorptive parts using the Kramers-Kronig relations,

$$\sigma_{aa}^2(\omega) = -\frac{2\omega}{\pi} P \int_0^\infty \frac{\sigma_{aa}^1(\omega')}{\omega'^2 - \omega^2} d\omega', \quad (5)$$

$$\sigma_{xy}^1(\omega) = \frac{2}{\pi} P \int_0^\infty \frac{\omega' \sigma_{xy}^2(\omega')}{\omega'^2 - \omega^2} d\omega', \quad (6)$$

where P denotes the principal value. The quasiparticle lifetime effect is taken into account by convoluting the optical conductivity spectra with a Lorentzian of line width Γ . For layered van der Waals materials such as graphite, the Γ is about 0.1 eV, (see Fig.1(a)(b) in [43]), which is also used in this paper.

For bulk magnetic material, the complex polar Kerr rotation angle is given by [29, 44]

$$\theta_K + i\epsilon_K = \frac{-\sigma_{xy}}{\sigma_{xx} \sqrt{1 + i(4\pi/\omega)\sigma_{xx}}}. \quad (7)$$

However, for a magnetic thin film on a nonmagnetic substrate, the complex polar Kerr rotation is given by [45–47]

$$\theta_K + i\epsilon_K = i \frac{2\omega d}{c} \frac{\sigma_{xy}}{\epsilon_{xx}^s} = \frac{8\pi d}{c} \frac{\sigma_{xy}}{(1 - \epsilon_{xx}^s)}, \quad (8)$$

where d stands for the thickness of the magnetic layer and ϵ_{xx}^s (σ_{xx}^s) the diagonal part of the dielectric constant (optical conductivity) of the substrate. Here we consider a SiO₂/Si substrate [3, 15], therefore the dielectric constant of bulk SiO₂ ($\epsilon_{ss}^s = 2.25$) is used here. Similarly, the complex Faraday rotation angle for a thin film can be written as [48]

$$\theta_F + i\epsilon_F = \frac{\omega d}{2c} (n_+ - n_-), \quad (9)$$

where n_+ and n_- represent the refractive indices for left- and right- polarized lights, respectively. The refractive indices are related to the optical conductivity and the dielectric function via expression $n_{\pm}^2 = \epsilon_{\pm} = 1 + \frac{4\pi i}{\omega} \sigma_{\pm} = 1 + \frac{4\pi i}{\omega} (\sigma_{xx} \pm i\sigma_{xy})$. Here the real parts of the optical conductivity σ_{\pm} can be written as

$$\sigma_{\pm}^1(\omega) = \frac{\pi e^2}{\hbar\omega m^2} \sum_{i,j} \int_{BZ} \frac{dk}{(2\pi)^3} |\Pi_{ij}^{\pm}|^2 \delta(\epsilon_{kj} - \epsilon_{ki} - \hbar\omega), \quad (10)$$

where $\Pi_{ij}^{\pm} = \langle \mathbf{k}j | \frac{1}{\sqrt{2}}(\hat{p}_x \pm i\hat{p}_y) | \mathbf{k}i \rangle$. Clearly, $\sigma_{xy} = \frac{1}{2i}(\sigma_+ - \sigma_-)$ and therefore σ_{xy} would be nonzero only if σ_+ and σ_- are different. In other words, magnetic circular dichroism is the fundamental cause of the nonzero σ_{xy} and hence the magneto-optical effect.

III. RESULTS AND DISCUSSION

A. Magnetic moments and magnetic anisotropy energy

Various magnetometer measurements and neutron scattering experiments have claimed a ferromagnetic ground state for bulk and thin film Fe₃GeTe₂ [8, 49–52]. Thus in this paper we consider a ferromagnetic ground state for bulk and few layers Fe₃GeTe₂. Calculated total and atomic spin (orbital) magnetic moments of bulk and 1-3 layers Fe₃GeTe₂ are listed in Table I, together with results of related works. By first glance, we observe similar total and atomic magnetic moments between 1-3 layers and bulk Fe₃GeTe₂ with discrepancy of spin magnetic moment within 0.05 μ_B . Thus, for the following paragraph we only discuss the magnetic properties of bulk Fe₃GeTe₂.

For bulk Fe₃GeTe₂, two different Fe sites have spin magnetic moments of 2.41 and 1.53 μ_B for FeI and FeII

(see Fig. 1) sites respectively. The local magnetic moments are in good agreement with the neutron scattering data [50](Table I). The spin magnetic moment difference between two sites is nearly 1 μ_B , indicating FeII site to hold an extra valence electron than the FeI site. This is highly possible due to the fully occupied spin-up $3d$ orbitals which can be seen in Fig. 3(b)(c) [53]. This is analogous to the relation between metal Fe, Co, and Ni where the extra valence electron give rise to 1 μ_B difference in spin magnetic moments [53]. Furthermore, the calculated orbital magnetic moments for Fe sites (FeI: 0.076 μ_B /Fe; FeII: 0.033 μ_B /Fe) are negligibly small (Table I) compared to that of spin magnetic moments. The average orbital magnetic moment is 0.062 μ_B /Fe, which is in good agreement with the XMCD measurement of magnitude 0.1 μ_B /Fe [51]. Notably, the orbital magnetic moment is comparable to that of spin magnetic moment on the Te site. Moreover, the Ge site holds a significant spin magnetic moment of -0.1 μ_B antiparallel to that of neighbouring Fe sites. In total, these result in a total spin magnetic moment of 6.29 μ_B , which is slightly higher than experimental bulk magnetization. Our calculated total magnetic moments appear to be 1.4 times larger than previous *ab initio* calculations [16, 17]. This is attributed to the fact that LDA method was used in their study [16, 17] instead of GGA method. However, our calculated local magnetic moments agree well with neutron scattering data. Adding on the fact that the band structures calculated by PBE pseudopotential is in good agreement with previous calculations and ARPES measurement [11, 54], this gives the validity to GGA exchange-correlation on depicting the magnetic structure of Fe₃GeTe₂ used in this paper.

The magnetic anisotropy energy (MAE) consists of the magnetocrystalline anisotropy energy (C-MAE) and the magnetic dipolar anisotropy (D-MAE). Results of C-MAE, D-MAE, and their sum MAE are listed in Table I. A positive value will indicate an out-of-plane magnetization easy axis by $\Delta E = E^{[100]} - E^{[001]}$. Thus, the negative D-MAE shown in Table I prefers an in-plane magnetization, which is expected for 2D systems. Furthermore, we notice that 1-3 layers Fe₃GeTe₂ have D-MAE larger of magnitude compared to that of bulk Fe₃GeTe₂. This is due to the 2D atomic structure of atomically thin Fe₃GeTe₂ [22, 31]. Since the D-MAE should be zero for an isotropic cubic, the slight value of D-MAE in bulk Fe₃GeTe₂ reflects the quasi-2D crystal structure of bulk Fe₃GeTe₂ (see Fig. 1). The calculated D-MAE for ML Fe₃GeTe₂ is higher than previous DFT calculation [17] with both preferring an in-plane magnetization. The difference in values is because of the different pseudopotential used where in our case PBE results in higher magnetic moments. Nevertheless, from Table I, we can see that the C-MAEs for 1-3 layers and bulk Fe₃GeTe₂ all exceed positive 3 meV/f.u, which is nearly ten times the value to the D-MAE. This indicates that C-MAE dominates the MAE contribution. The calculated C-MAE can relate to the calculated orbital magnetic moments

TABLE I. Total spin magnetic moment (m_t^s), atomic (averaged) spin magnetic moment ($m_{FeI}^s, m_{FeII}^s, m_{Ge}^s, m_{Te}^s$), and orbital magnetic moment ($m_{FeI}^o, m_{FeII}^o, m_{Ge}^o, m_{Te}^o$), as well as the calculated magneto-crystalline anisotropy (ΔE_c), dipolar anisotropy energy (ΔE_d) and the total magnetic anisotropy energy ($\Delta E_{ma} = \Delta E_c + \Delta E_d$) of bulk and 1-3 layers Fe_3GeTe_2 . Positive ΔE_c indicates an favoured out-of-plane magnetization. Also, the local spin and orbital moment for in-plane magnetization of bulk Fe_3GeTe_2 is listed (bulk [100]). Earlier experimental values of SQUID, neutron scattering and RMCD experiments are listed for comparison.

Structure	m_t^s ($\mu_B/f.u.$)	$m_{FeI}^s(m_{FeI}^o)$ ($\mu_B/atom$)	$m_{FeII}^s(m_{FeII}^o)$ ($\mu_B/atom$)	$m_{Ge}^s(m_{Ge}^o)$ ($\mu_B/atom$)	$m_{Te}^s(m_{Te}^o)$ ($\mu_B/atom$)	ΔE_c (ΔE_d) (meV/f.u.)	ΔE_{ma} (meV/f.u.)
monolayer	6.27	2.44 (0.076)	1.47 (0.033)	-0.10 (0.001)	-0.04 (-0.018)	3.00 (-0.317)	2.68
bilayer	6.31	2.43 (0.076)	1.54 (0.033)	-0.10 (0.001)	-0.04 (-0.017)	3.02 (-0.326)	2.69
trilayer	6.31	2.43 (0.076)	1.54 (0.032)	-0.10 (0.001)	-0.04 (-0.017)	3.20 (-0.325)	2.88
bulk	6.29	2.41 (0.075)	1.53 (0.030)	-0.10 (0.001)	-0.04 (-0.016)	3.41 (-0.086)	3.32
bulk [100]	6.29	2.41 (0.084)	1.54 (0.050)	-0.10 (0.002)	-0.04 (-0.006)	-	-
bulk	3.96 ^a , 4.875 ^b	2.18 ^c (-)	1.54 ^c (-)	-	-	$\sim 3.4^d$	-
monolayer	-	-	-	-	-	2.76 ^e (-0.108 ^e)	2.0 ^f , 2.7 ^g

^aReference[50] (SQUID experiment); ^bReference[8] (SQUID experiment); ^cReference [50] (Neutron scattering experiment at 4K); ^dReference[19](DFT); ^eReference [17](DFT); ^fReference [3](RMCD experiment); ^gReference [18](DFT)

because both physical phenomenon are caused by the SOC [20]. From Table I, we can compare the magnetic moments of bulk Fe_3GeTe_2 between in-plane and out-of-plane magnetization (bulk versus bulk[100]). While the spin magnetic moments remain the same, the orbital magnetic moments on the heavy element Te site are larger under out-of-plane magnetization. Thus, the large C-MAE of Fe_3GeTe_2 originates from the SOC introduced by the heavy element Te.

From Table I, we can see that the MAE increases as the number of layers increases. The MAE of ML Fe_3GeTe_2 is 2.68 meV/f.u., which is in good agreement with experimental date (2.0 meV/f.u.) measured by RMCD experiment [3]. On the other hand, bulk Fe_3GeTe_2 has the largest MAE with the value of 3.32 meV/f.u., corresponding to roughly 1.11 meV/3d atom. The MAEs for Fe_3GeTe_2 systems are large and more importantly prefer the out-of-plane magnetization. In detail, the MAEs for 1-3 layers and bulk Fe_3GeTe_2 are nearly three orders of magnitude larger than that of elemental ferromagnets Fe and Ni ($5\mu eV/f.u.$) [55]. They are also two to five times of magnitude larger than the other two atomically thin ferromagnets $Cr_2Ge_2Te_6$ (0.4 meV/f.u.) [22] and CrI_3 (0.5 meV/f.u.)[31]. Remarkably, the calculated MAEs of Fe_3GeTe_2 systems are larger of magnitude to magnetic heavy metal alloys that are famous for large MAE, such as FePt (-2.75 meV/f.u.) or CoPt (-0.97 meV/f.u.) [56]. Even experimental measured MAE for ML Fe_3GeTe_2 (2.0 meV/f.u.) is larger than that of measured MAE for FePt (-1.2 meV/f.u.) and CoPt (-1.0 meV/f.u.) [57]. Overall, the large anisotropy energy suggests that few layers Fe_3GeTe_2 could have appreciable application in high density data storage.

B. Electronic structure

The optical and the magneto-optical properties can be obtained directly from the electronic structure. There-

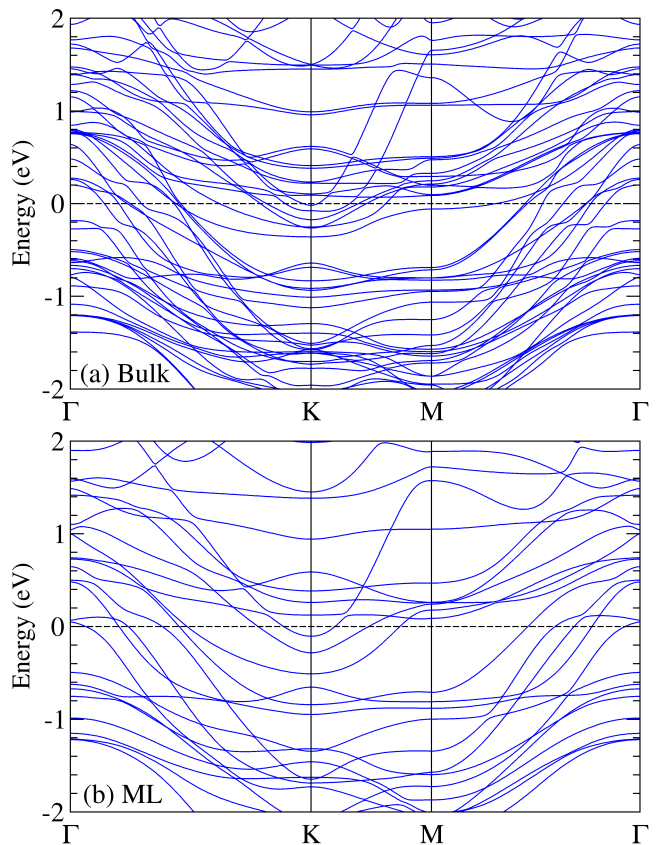


FIG. 2. Relativistic band structures of (a) bulk and (b) ML Fe_3GeTe_2 in ferromagnetic state with out-of-plane magnetization. The Fermi level is shifted to 0 eV.

fore, we calculate the relativistic band structures of 1-3 layers and bulk Fe_3GeTe_2 , as displayed in Fig. 2,S1. We can identify the metallic nature from band crossings through Fermi level in all structures Fe_3GeTe_2 . We also observe similar patterns between each band structures (Fig. 2,S1). For example, downward concaves appear

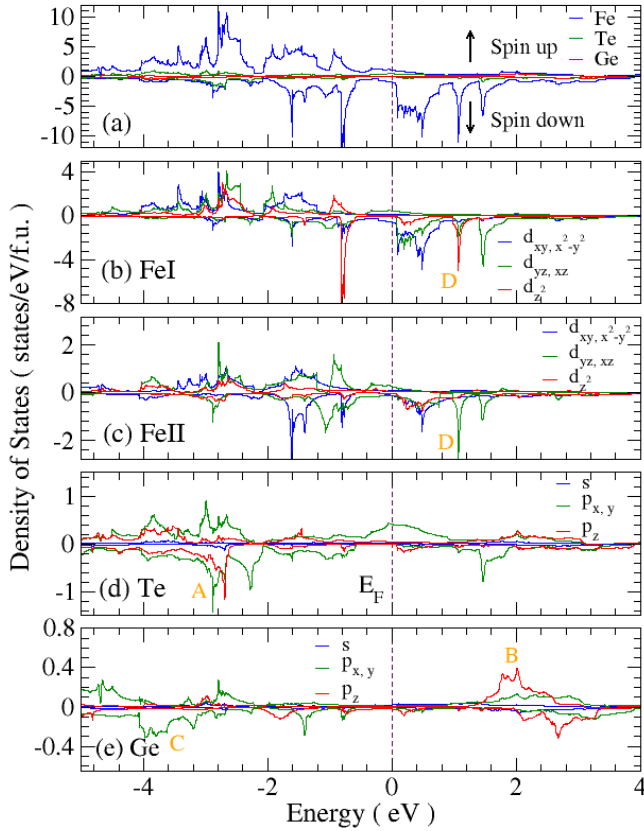


FIG. 3. Scalar relativistic site-, orbital-, and spin-projected DOS of ferromagnetic bulk Fe_3GeTe_2 . The Fermi level is shifted to 0 eV.

around Γ point and upward concaves appear around K point. Increase in layers introduces extra states with similar eigenvalues at similar positions in the Brillouin zone. This suggests a weak interlayer coupling that is due to the layered structure of Fe_3GeTe_2 . We can imagine every layer to be isolated and thus nearly identical states would appear in the band structures. This could also explain the similarity of density of states (DOS) between 1-3 layers and bulk Fe_3GeTe_2 (Fig. 3,4,S2,S3).

Next, in order to understand the spin behaviour, we take a look into the total as well as site-, orbital-, and spin-projected DOS for 1-3 layers and bulk Fe_3GeTe_2 . The result is displayed in Fig. 3,4,S2,S3. For bulk Fe_3GeTe_2 (see Fig. 3), we can see that the lower valence bands ranging from -5.0 to -2.2 eV originate from the hybridization between Fe d , Ge and Te p orbitals. The upper valence bands from -2.2 eV to lower conduction bands of 1.0 eV are dominated mainly by Fe d orbitals with minor contributions of Te p orbitals around the Fermi level. Furthermore, from Fig. 3(b)(c), we observe fully occupied spin-up Fe d bands, indicating a strong exchange splitting in bulk Fe_3GeTe_2 . Notably, the DOS is different between two Fe sites even though both Fe sites have fully occupied spin-up d states. On the FeI sites, the broad peaks are mainly originated from occupied spin-

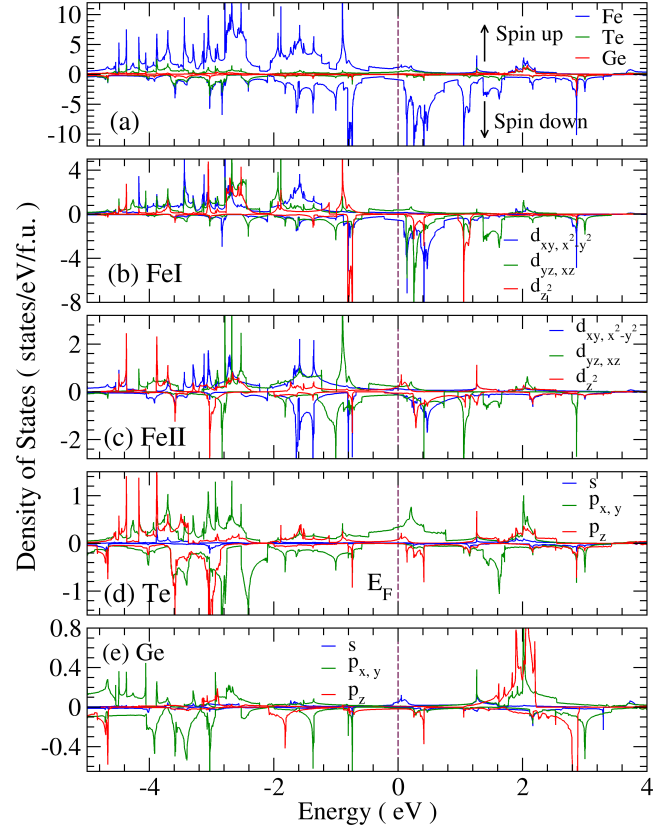


FIG. 4. Scalar relativistic site-, orbital-, and spin-projected DOS of ferromagnetic monolayer Fe_3GeTe_2 . The Fermi level is shifted to 0 eV.

down d_{z^2} orbitals. On the FeII sites, the broad peaks are mainly made up of occupied spin-down $d_{xy, x^2-y^2, yz, xz}$ orbitals. Interestingly, more peaks of spin-down DOS on FeII sites compared to that on FeI sites can echo with previous results regarding local magnetic moments. The extra valence electron on the FeII site leads to a $1 \mu_B$ less in local spin magnetic moments compared to that on the FeI site. By integrating the spin-down DOS below Fermi level, we also result in $1.8 \mu_B/\text{FeI}$ and $2.3 \mu_B/\text{FeII}$, which agrees with such argument.

In other words, on the FeI site, d_{z^2} state is energetically favoured and thus occupied first. On the FeII site, d_{z^2} is of higher energy state and thus occupied last. In crystal field theory, d orbitals aligned with the ligands would require more energy to be occupied due to the repulsion force. Therefore, as seen from Fig. 1(a)(c), FeI sites do not have ligands along c direction, and thus the d_{z^2} state has the lowest energy. On the other hand, we can observe the structure around FeII (Fig. 1(a)) to find a trigonal bipyramidal structure formed by a triangular bonding between FeII-Ge (repulses d_{xy, x^2-y^2} orbitals) and a linear bonding between FeII-Te (repulses d_{z^2}). Also, FeI-FeII bonds also form a triangular prism, which repulses $d_{yz, xz}$ orbitals. Therefore, by atomic structure, we can not distinguish the energy level difference between d states on

the FeII site. Nonetheless, as displayed in Fig. 3(c), there are no peaks of spin-down d_{z^2} orbitals on the FeII site in the valence bands. Thus we can conclude that the FeII-Te linear bonding is of the strongest among all.

The site-, orbital-, and spin- projected DOSs of ML Fe_3GeTe_2 are shown in Fig. 4. The features of the DOS spectra of ML Fe_3GeTe_2 are similar to that of bulk Fe_3GeTe_2 . The main difference is the enhancement in peaks of FeII d_{z^2} orbitals and Ge, Te p_z orbitals at lower valence bands and at high conduction bands. This is due to the lessen of interlayer coupling for 2D materials. The decrease in repulsion force along c direction allows FeII d_{z^2} orbitals and Ge, Te p_z orbitals to be occupied first. In contrast, the peaks of d_{z^2} orbital on FeI sites are the same for bulk and ML Fe_3GeTe_2 because no ligands are along c direction. The site-, orbital-, and spin- projected DOSs of BL and TL Fe_3GeTe_2 are shown in Fig. S2,S3 where the spectra fall in between that of ML and bulk Fe_3GeTe_2 .

With results of orbital-projected DOS, we can draw our attention once again to the C-MAE which is caused by the interplay between the SOC and the crystal field. The theoretical treatment of heavy element Te, where the SOC is larger than the crystal field [58], is discussed in previous subsection where we show large difference in orbital magnetic moments (Table I). However, for half filled d orbitals, crystalline fields are stronger than the SOC. Through perturbation theory analysis, we can conclude that the coupling of SOC between the occupied and unoccupied Fe d states near the Fermi level contributes significantly to the C-MAE [58]. In particular, for Fe_3GeTe_2 systems, the exchange splitting is large enough for spin-up bands to be fully occupied. Thus, the coupling between (un)occupied spin-down orbitals would be significant [58]. The SOC matrix elements $\langle d_{xy} | H_{SO} | d_{x^2-y^2} \rangle$ and $\langle d_{yz} | H_{SO} | d_{xz} \rangle$ prefer the out-of-plane anisotropy, while $\langle d_{yz} | H_{SO} | d_{xy} \rangle$, $\langle d_{yz} | H_{SO} | d_{z^2} \rangle$, and $\langle d_{yz} | H_{SO} | d_{x^2-y^2} \rangle$ favour an in-plane anisotropy [58, 59]. Through relativistic calculations, the ratios of these matrix elements on the FeI site are $\langle d_{xy} | H_{SO} | d_{x^2-y^2} \rangle^2 : \langle d_{yz} | H_{SO} | d_{xz} \rangle^2 : \langle d_{yz} | H_{SO} | d_{xy} \rangle^2 : \langle d_{yz} | H_{SO} | d_{z^2} \rangle^2 : \langle d_{yz} | H_{SO} | d_{x^2-y^2} \rangle^2 = 5 : 1 : 2 : 4 : 2$; while on the FeII site are of ratios $\langle d_{xy} | H_{SO} | d_{x^2-y^2} \rangle^2 : \langle d_{yz} | H_{SO} | d_{xz} \rangle^2 : \langle d_{yz} | H_{SO} | d_{xy} \rangle^2 : \langle d_{yz} | H_{SO} | d_{z^2} \rangle^2 : \langle d_{yz} | H_{SO} | d_{x^2-y^2} \rangle^2 = 4 : 2 : 1 : 2 : 1$. Figure 3, 4, S1, S2 show that in 1-3 layers and bulk Fe_3GeTe_2 , FeI site has prominent peaks of all d orbitals around the Fermi level. This supports both $\langle d_{xy} | H_{SO} | d_{x^2-y^2} \rangle^2$ and $\langle d_{yz} | H_{SO} | d_{z^2} \rangle^2$ to compete each other regarding anisotropy. However, on the FeII site, the missing of d_{z^2} peak around Fermi level leads to little contribution of $\langle d_{yz} | H_{SO} | d_{z^2} \rangle^2$ toward C-MAE. Clearly, the C-MAE is dominated by $\langle d_{xy} | H_{SO} | d_{x^2-y^2} \rangle^2$ term on the FeII site that supports a out-of-plane anisotropy. We recall that in previous paragraph we have argued a stronger bonding between FeII-Te from the DOS spectra. Thus, we shall conclude that

the strong out-of-plane anisotropy originates from FeII and Te sites for 1-3 layers and bulk Fe_3GeTe_2 .

C. Optical and magneto-optical conductivity

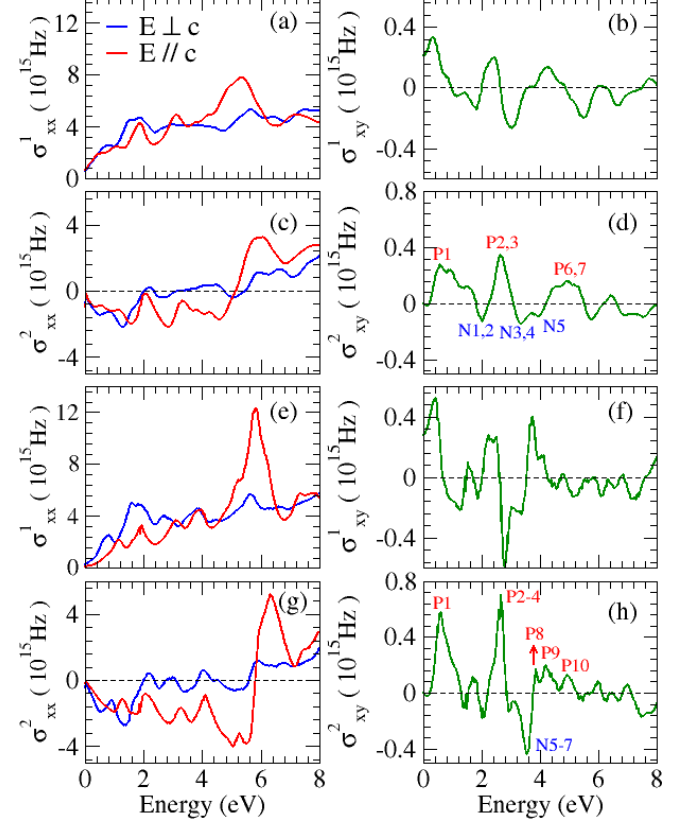


FIG. 5. Real (a)[(e)] diagonal and (b)[(f)] off-diagonal, imaginary (c)[(g)] diagonal components and (d)[(h)] off-diagonal components of the optical conductivity tensor of bulk [ML] Fe_3GeTe_2 in ferromagnetic state with an out-of-plane magnetization. All the spectra have been convoluted with a Lorentzian of 0.1 eV to simulate the finite electron lifetime effects.

Here we calculate the optical and magneto-optical conductivity tensors for 1-3 layers and bulk Fe_3GeTe_2 . The results are displayed in Fig. 5 and S4. We can see that all spectra have similar shape between different structures with ML having slightly sharper peaks. The similarity is due to the weak interlayer vdW interaction among layered materials. Such behaviour is also reported in other layered vdW materials like CrI_3 and $\text{Cr}_2\text{Ge}_2\text{Te}_6$ [22, 31]. For the following section, we would perform analysis onto ML and bulk Fe_3GeTe_2 . Firstly, the diagonal part of the optical conductivity σ_{xx} and σ_{zz} differ significantly (see Fig. 5(a)(e)). The σ_{xx} indicates the response to an in-plane electric field polarization ($E \perp c$) and the σ_{zz} indicates the response to an out-of-plane electric field polarization ($E \parallel c$). In detail, for bulk Fe_3GeTe_2

(Fig. 5(a)), the absorptive part of the diagonal term σ_{xx}^1 is larger than σ_{zz}^1 in low energy region of 0.0-3.0 eV, while being similar at 3.0-4.4 eV, and finally smaller at high energy region at 4.4-6.0 eV. Both $\sigma_{xx,zz}^1$ show an oscillating behaviour after 6.0 eV and gradually become similar till 8.0 eV. ML Fe_3GeTe_2 obtains similar deviation between σ_{xx}^1 and σ_{zz}^1 but larger in magnitude, indicating a larger optical anisotropy. Such obvious optical anisotropy can be expected for 2D or quasi-2D structural materials [22, 31] and can be further explained by means of orbital-projected DOS spectrum. Note that the $p_{x,y}$ and d_{xy,x^2-y^2} (p_z and d_{z^2}) states can only be excited by $E \perp c$ ($E||c$) polarized light while $d_{xz,yz}$ can be excited by both. From Fig. 3,4, the upper valence bands are contributed by Fe d and Ge, Te p orbitals. From energy region -3.0 to 0.0 eV, shown in Fig. 3, 4, the overall weight of Fe d orbitals that would trigger the optical anisotropy are balanced between FeI d_{z^2} orbitals (excited by $E||c$) and FeII d_{xy,x^2-y^2} orbitals (excited by $E \perp c$). However, broad peaks of $p_{x,y}$ introduced by the Te site explains the slight higher peaks of σ_{xx}^1 in energy region below 3.0 eV (Fig. 5(a)(e)). Furthermore, significant FeII d_{z^2} and Te p_z states appear at higher energy region from -5.0 to -3.0 eV. ML Fe_3GeTe_2 has in particular a large Te p_z peak due to the loosen of interlayer coupling (see Fig. 4(c)(d)). This explains firstly the rising of σ_{zz}^1 ($E||c$) above 4.4 eV and secondly the reason for ML Fe_3GeTe_2 to obtain the largest optical anisotropy among all structures.

Overall, for bulk and ML Fe_3GeTe_2 , σ_{xx}^1 features a quick rising from 0.0 eV to 1.6 eV, and then an oscillating as well as rising behaviour till 8.0 eV. σ_{zz}^1 , on the other hand, increases all the way to 5.4 eV (5.8 eV) for bulk (ML) Fe_3GeTe_2 with few local peaks along the way. Then, a drastic drop happens till 6.8 eV followed by a monotonically decrease till 8.0 eV. The dispersive spectrum for diagonal component $\sigma_{xx,zz}^2$ generally follows that of absorptive part but with a decreasing start. A sign change for σ_{zz}^2 at 5.2 eV (5.8 eV) can be seen for $\sigma_{xx,zz}^2$ of bulk (ML) Fe_3GeTe_2 .

The calculated real (σ_{xy}^1) and imaginary (σ_{xy}^2) parts of the off-diagonal optical conductivity components are displayed in Fig. 5(b)(d) for bulk and (f)(h) for ML Fe_3GeTe_2 . First of all, note that the dc-limit for σ_{xy}^1 is actually the anomalous Hall conductivity which can be evaluated through Brillouin zone integration of Berry curvature [25, 26]. Through proper conversion, we obtain the anomalous Hall conductivity of values 233 S/cm, 312 S/cm, 241 S/cm, and 287 S/cm for bulk and ML, BL, and TL Fe_3GeTe_2 , respectively. The dc-limit for bulk Fe_3GeTe_2 σ_{xy}^1 spectrum agrees quite well with few related works on anomalous Hall conductivity with ~ 360 S/cm [13] and ~ 287 S/cm [12] for experimental and theoretical work, respectively. Secondly, bulk and ML Fe_3GeTe_2 have similar patterns for the off-diagonal conductivity spectrum (σ_{xy}). For both structures, the off-diagonal spectrum oscillates with ML Fe_3GeTe_2 featuring sharper and higher peaks. Prominent peaks occur mostly at 0.0 to 4.4 eV while after 4.4 eV the values are nearly zero, in-

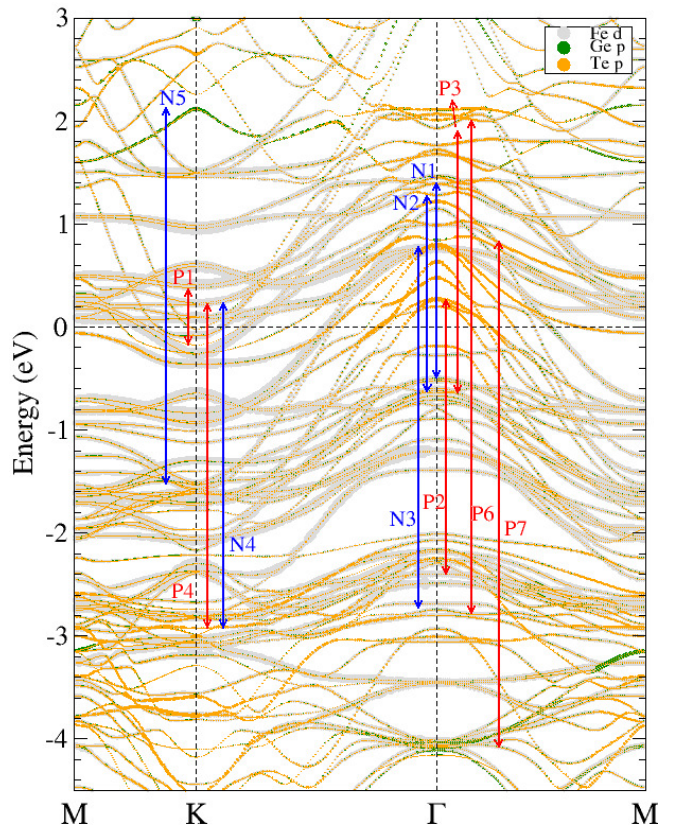


FIG. 6. Relativistic site- and orbital- projected band structures of ferromagnetic bulk Fe_3GeTe_2 . The Fermi level is shifted to 0 eV. The principal interband transitions at Γ and K point, as well as the corresponding peaks in the σ_{xy} spectrum in Fig. 5(d) are indicated by red and blue arrows.

dicating very little magnetic circular dichroism. Thirdly, the imaginary part of the off-diagonal optical conductivity σ_{xy}^2 represents the absorption difference between left- and right- circular light. As displayed in Fig. 5(d)(h), the major difference in σ_{xy}^2 between bulk and ML Fe_3GeTe_2 spectrum happens at 1.2 eV. σ_{xy}^2 of ML Fe_3GeTe_2 drops drastically at 1.2 eV while σ_{xy}^2 of bulk Fe_3GeTe_2 remains positive from 1.2 - 1.5 eV. As for higher energy regions, σ_{xy}^2 of ML Fe_3GeTe_2 features obvious oscillating behaviour near zero response while that of bulk Fe_3GeTe_2 still has several peaks.

In detail, for ML Fe_3GeTe_2 , σ_{xy}^1 has prominent positive peaks at 0.4 eV and 3.8 eV as well as a negative peak at 2.8 eV. For σ_{xy}^2 , ML Fe_3GeTe_2 has large positive peaks at 0.6 eV and 2.6 eV as well as a large negative peak at 3.6 eV. In comparison, bulk Fe_3GeTe_2 has peak positions identical to ML for both σ_{xy} spectra. However, a significant shrinkage of the negative peak at 3.6 eV can be observed for bulk Fe_3GeTe_2 .

According to Eq. (3), (4), (10), the absorptive parts of the optical conductivity elements (σ_{xx}^1 , σ_{zz}^1 , σ_{xy}^2 , σ_{\pm}^1) are directly related to the dipole-allowed interband transitions. This depicts the physical origin of the promi-

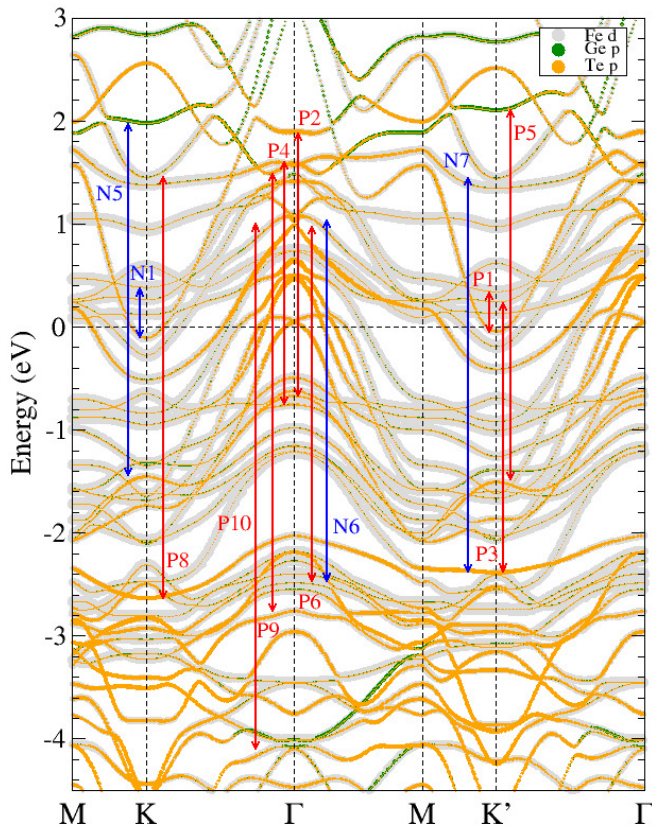


FIG. 7. Relativistic site- and orbital- projected band structures of ferromagnetic monolayer Fe_3GeTe_2 . The Fermi level is shifted to 0 eV. The principal interband transitions at Γ , K and K' point, as well as the corresponding peaks in the σ_{xy} spectrum in Fig. 5(h) are indicated by red and blue arrows.

nent peaks of the optical spectra and allows us to understand the dipole selection rule for our material or the ones that obtain similar symmetry. Fig. 6 and 7 are the results of the main dipole-allowed optical transitions of bulk and ML Fe_3GeTe_2 plotted on the site- and orbital-projected relativistic band structures. Based on the transition matrix elements and the derived selection rules, we have assigned the peaks of the absorptive part of the magnetic-optical conductivity σ_{xy}^2 (see Fig. 5(d)(h)) to the corresponding optical transitions indicated with red and blue symbols and arrows on Fig. 6 and 7. Details regarding symmetry analysis, dipole selection rules can be found in the supplementary material.

Following previous studies on dipole selection rules for 2D materials $\text{Cr}_2\text{Ge}_2\text{Te}_6$ [22] and CrI_3 [31], we have applied symmetry analysis on the Γ -point of the relativistic band structures of bulk and ML Fe_3GeTe_2 . However, we discover that only with the inclusion of K-point could the prominent peak at 0.4 eV of Fig. 5(d)(h) (P1 peak) as well as few local peaks throughout the spectrum (N5 peak of Fig. 5(d) and P8 peak of Fig. 5(h)) be assigned. The necessity of including K-point could be due to the following two reasons. One, for a hexagonal Brillouin

zone (see Fig. 1(b)), Γ and K-point are two points that obtain the highest symmetry. This introduces symmetry protected degeneracies in the absence of the SOC [11]. Such degeneracies would be lifted with the inclusion of the SOC and the splitted bands would obtain different irreducible representations (irrep.). Consequently, by the dipole selection rule, the different irrep. would result in different transitions regarding left- and right-circular polarized light and thus the magnetic circular dichroism (ie. P6, N6 in Fig. 7 and Table S2.). Two, from the relativistic band structures displayed in Fig. 2, we can see that Γ and K-point are usually where band maximum or minimum occur. Such band extrema are usually flat bands that generate large joint density of states. This gives rise to prominent optical transitions. Note that due to inversion symmetry break for odd layers Fe_3GeTe_2 (see Fig.1(a)), K' point of ML Fe_3GeTe_2 is also included and would be further discussed in the following paragraph.

From Fig. 6 and 7, we can see that both bulk and ML Fe_3GeTe_2 have main transitions at the region of -4 eV to 2.0 eV. This coincides with the main peaks of the σ_{xy}^2 at 0.0 - 4.4 eV (Fig. 5(d)(h)). Interestingly, we discover that under a full dominance of Fe d orbitals from -4.4 eV to 2.0 eV, large optical transitions would only arise from states where Te p and Ge p orbitals are hybridized in. This could link to the calculated DOS spectra from previous section. For example, peak P6 of σ_{xy}^2 for bulk Fe_3GeTe_2 (Fig. 5(d)) originates mainly from an optical transition from ~ -3.0 eV to ~ 2.0 eV (Fig. 6), and also coincides with the Te peak A to Ge peak B from Fig. 3(d)(e). Following the same fashion, peak P7 of bulk Fe_3GeTe_2 (Fig. 5(d)) originates mainly from an optical transition from ~ -4.0 eV to ~ 0.8 eV (Fig. 6), and also coincides with the Ge peak C to FeI,II peak D from Fig. 3(b)(e). The same thing can be seen in ML Fe_3GeTe_2 since the DOS spectra between structures do not differ too much.

Moreover, from Fig. 6 and 7, we could see that pairs of right- and left-circular dipole allowed transitions would appear such as peaks P4, N4 in Fig. 6 for bulk and peak P6, N6 in Fig. 7 for ML Fe_3GeTe_2 . This is due to broken degeneracies leading to different irreps and thus difference in left- or right-handed circular light transitions. From Table S4 and S5 we could directly observe the magnetic circular dichroism by sign and value differences of the transition matrix elements. Furthermore, we can see that from Fig. 7, optical transitions of ML Fe_3GeTe_2 sometimes come in pairs regarding K and K' point such as peaks N1, P1 and peaks N5, P5 at Fig. 7. This is the consequence of inversion symmetry break which leads to an interchange of irreps between K and K' -point. Such behaviour is similar to the concept of recently reported ferrowalley materials where the SOC and an exchange field drives the material to become valley-polarized [66]. Thus, possible valley-polarized effect could be discovered in odd layers Fe_3GeTe_2 . Nevertheless, the similarity between σ_{xy}^2 among different structures (Fig. 5(d)(h), S4(d)(h)) is still observed through our results. We could then con-

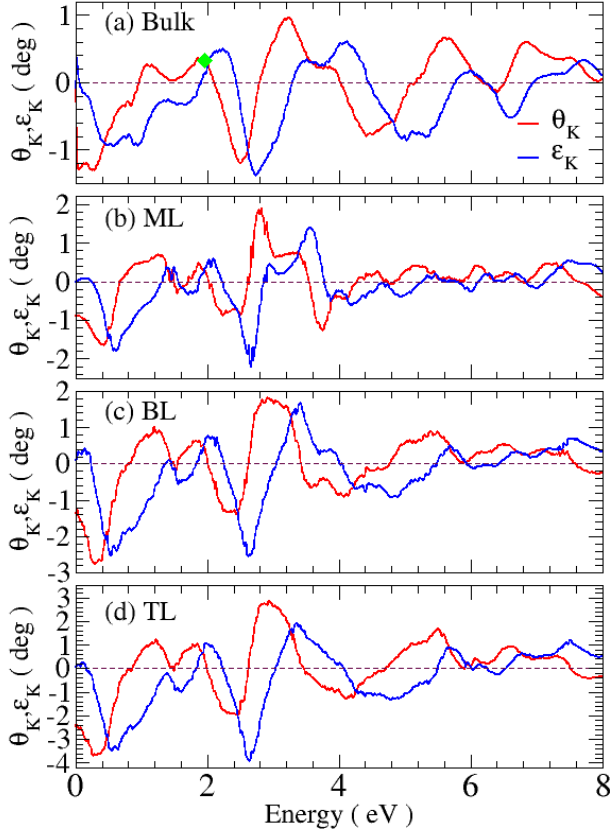


FIG. 8. Kerr rotation (θ_K) and ellipticity (ϵ_K) spectra for (a) bulk, (b) ML, (c) BL, and (d) TL Fe_3GeTe_2 in ferromagnetic state with an out-of-plane magnetization. Green diamond denotes the θ_K value of available experiment measurement [15].

clude that although inversion symmetry breaking affects the transition matrix elements at K and K' point, it does not affect the magneto-optical spectrum. Similar effects is shown in CrI_3 with different stacking order to have minor changes in optical spectrum [31].

To summarize, by symmetry analysis of Γ , K, and K'-point of bulk and ML Fe_3GeTe_2 , we have identified the effect of inversion symmetry breaking and proposed possible valley-polarized effect happening in odd layers Fe_3GeTe_2 systems. Regardless, different symmetry does not directly affect the MO spectrum. The crucial factor of the MO spectrum is the hybridization between heavy elements and the half-filled d orbitals which introduce magnetism.

D. Magneto-optical Kerr and Faraday effects

The polar MO Kerr and Faraday rotation spectrum are calculated from the optical conductivity spectrum via Eq. 5-7, and the results are shown in Figs. 8,9. Note that for atomically thin Fe_3GeTe_2 , we would need to consider the effect of the substrate. In our case we have considered a

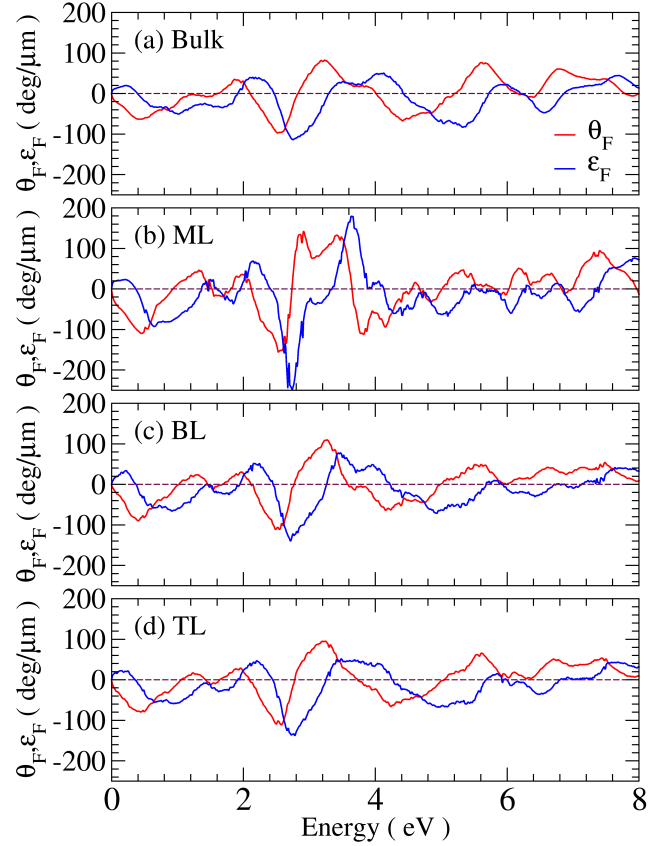


FIG. 9. Faraday rotation (θ_F) and ellipticity (ϵ_F) spectra for (a) bulk, (b) ML, (c) BL, and (d) TL Fe_3GeTe_2 in ferromagnetic state with an out-of-plane magnetization.

SiO_2 substrate with a dielectric constant of $\epsilon_{xx}^s = 2.25$ (Eq.8). From Eq.8, we could see that the MO Kerr rotation and ellipticity is directly related to σ_{xy} with a minus sign and to be divided by a constant of the substrate's dielectric constant. Therefore, we could see the resemblance between Fig. 5,S2, and Fig. 8 where the MO Kerr rotation (θ_K) and Kerr ellipticity (ϵ_K) spectra of 1-3 layers Fe_3GeTe_2 nearly follows that of σ_{xy}^1 and σ_{xy}^2 , respectively. As for bulk Fe_3GeTe_2 , higher peaks can occur if the σ_{xx} spectrum has relatively low value because σ_{xx} is the denominator in Eq. 7. However, due to the metallic nature of Fe_3GeTe_2 , the absorptive part of the diagonal element σ_{xx}^1 has a finite value throughout the whole energy region (Fig. 5(a)). Accordingly, the Kerr rotation spectrum of bulk Fe_3GeTe_2 will have similar pattern as that of σ_{xy}^1 , with values divided by that of σ_{xx}^1 . As for the Kerr ellipticity (ϵ_K), the pattern follows that of σ_{xy}^2 but with an extra peak at nearly 0.0 eV coming from the small value of σ_{xx}^2 at low energy region.

Throughout all structures of Fe_3GeTe_2 , the MO Kerr rotation spectra are alike due to the weak interlayer coupling. Generally, the Kerr rotation spectrum starts with a negative peak at ~ 0.4 eV and oscillates all the way to 4.0 eV. Prominent positive peaks are at ~ 1.2 eV, ~ 1.8 eV, and ~ 2.6 eV, while negative peaks are at ~ 0.4 eV,

and ~ 2.5 eV. For energy region above 4.0 eV, the MO Kerr rotation spectrum of ML Fe_3GeTe_2 oscillates with little response all the way to high energy region. In the case of bulk, BL and TL Fe_3GeTe_2 , few peaks are seen at ~ 5.6 eV for all considered structures and a peak at ~ 6.8 eV appears in particular for bulk Fe_3GeTe_2 . Remarkably, the maximum MO Kerr rotation angles are large in Fe_3GeTe_2 systems. Positive Kerr rotation maximum is 0.96° at 3.2 eV for bulk as well as 1.89° , 1.82° , and 2.70° for ML, BL, and TL at 2.8 eV, respectively. On the other hand, the negative Kerr rotation maximum is -1.30° at 0.25 eV for bulk as well as -1.65° , -2.76° , and -3.73° at 0.26 eV for ML, BL, and TL, respectively. These large Kerr angles and ellipticities suggest that atomically thin or bulk Fe_3GeTe_2 to be valuable in MO nanodevices.

To understand the potential of Fe_3GeTe_2 systems in the field of MO applications, we then compare the performance of Kerr rotation angles to several popular MO materials. We start with systems that are same as Fe_3GeTe_2 , which are the $3d$ transition ferromagnetic metals. Simple systems such as Fe, Co, Ni were first studied. Bcc Fe has a Kerr rotation of -0.5° at 1 eV; hcp Co has a Kerr rotation of -0.42° at 5 eV, and fcc Ni has a Kerr rotation of -0.25° at 4 eV [24, 29, 39]. Later, it was discovered that the MO Kerr rotation angles of $3d$ transition metal alloys containing heavy elements are large. Famous examples are FePt, CoPt, and PtMnSb with values ranging from 0.4° to 0.5° [29, 60]. The strong SOC of Pt plays an important role in such enhancement [30]. Among all $3d$ transition metals, thin film MnBi has a respectively large Kerr rotation of 2.3° at 1.84 eV [61]. Moreover, recent discoveries of antiferromagnetic metals were reported to have MOKE effect due to a noncollinear magnetic structure. For example, Mn_3Sn was experimented to have 0.02° at room temperature [62], and Mn_3Pt was theoretically proposed to have 0.6° at 0.7 eV [40]. Up to this point, we can see that among these traditional MO ferromagnetic metals or even theoretically proposed antiferromagnetic metals, bulk Fe_3GeTe_2 has a comparable MO Kerr rotation angle (-1.3° at 0.25 eV). Thin film Fe_3GeTe_2 have even better performances with TL Fe_3GeTe_2 in particular having exceptional MO Kerr rotation angle over 3° .

For comparison, we discuss shortly about some famous semiconductors with good MO properties. $\text{Y}_3\text{Fe}_5\text{O}_{12}$ and recently theoretically well-explained $\text{Bi}_3\text{Fe}_5\text{O}_{12}$ has Kerr rotation of -0.12° at 4.8 eV and -1.21° at 2.4 eV, respectively [63, 64]. As for diluted magnetic semiconductors $\text{Ga}_{1-x}\text{Mn}_x\text{As}$, a Kerr rotation of 0.4° near 1.8 eV was reported [65]. Moreover, two previously studied van der Waals 2D magnetic semiconductors $\text{Cr}_2\text{Ge}_2\text{Te}_6$ and CrI_3 have large Kerr rotation of 2.2° near 2.8 eV under TL structure and -2.1° at 4.3 eV under bulk form, respectively [22, 31]. Among current studies regarding 2D magnetic materials, the Kerr rotation of Fe_3GeTe_2 systems are not only comparable but even better in some structures such as BL and TL Fe_3GeTe_2 . Pronounced MO properties of Fe_3GeTe_2 suggest them to have promising applications

for MO sensors, or data-storage devices. Experimentally, MOKE measurements were done on a 340-nm thick sample using 633 nm HeNe laser, which is equivalent to a photon energy of 1.96 eV. The experimental measured Kerr angle $\sim 0.33^\circ$ is denoted as a green diamond on Fig. 8(a) [15]. A very good agreement further supports the predicted MO effects of 2D Fe_3GeTe_2 .

The complex MO Faraday rotation is also calculated for 1-3 layers and bulk Fe_3GeTe_2 with results shown in Fig. 9. The MO Faraday rotation spectra is similar to that of MO Kerr rotation spectra in all considered structures. Remarkably, we can observe large positive (negative) peaks of Faraday rotation of 82 (-97) $^\circ/\mu\text{m}$, 142 (-156) $^\circ/\mu\text{m}$, 109 (-111) $^\circ/\mu\text{m}$, and 95 (-111) $^\circ/\mu\text{m}$ at $\sim 2.55(3.0)\text{eV}$ for bulk, ML, BL, and TL Fe_3GeTe_2 , respectively. For comparison, MnBi thin films are known to possess the largest Faraday rotation angle of $\sim 80^\circ/\mu\text{m}$ at 1.77 eV. [48, 61]. As for widely used semiconductor $\text{Y}_3\text{Fe}_5\text{O}_{12}$, it possesses a Faraday rotation of $7.2^\circ/\mu\text{m}$ at 3.9 eV [64]. With the substitution of heavy element Bismuth, $\text{Bi}_3\text{Fe}_5\text{O}_{12}$ can obtain a Faraday rotation angle of $51.2^\circ/\mu\text{m}$ at 3.7 eV [64]. Notably, for recent studied 2D magnetic semiconductors, 2D $\text{Cr}_2\text{Ge}_2\text{Te}_6$ has a Faraday rotation angle of $\sim 120^\circ/\mu\text{m}$ [22] and 2D CrI_3 has a Faraday rotation angle of at most $\sim 108^\circ/\mu\text{m}$ [31]. Clearly, bulk and 2D Fe_3GeTe_2 reported here have better performances regarding Faraday rotation. Overall, the MO Kerr rotation and MO Faraday rotation of bulk or 2D Fe_3GeTe_2 are large (Fig. 8,9) which further suggest the promising application for magneto-optical devices.

IV. CONCLUSION

In conclusion, we have investigated the magnetic properties, electronic structures, optical and magneto-optical effects in 2D as well as bulk Fe_3GeTe_2 by first principle calculations based on the density functional theory. In particular, we focus on two relativity-induced properties of these 2D materials, namely, the MAE and MO effects. Firstly, large MAEs of ~ 3 meV/f.u. are found for all the considered structures. In particular, these large MAEs are comparable with that of FePt which has the largest MAE among the transition metal alloys. Such strong perpendicular MAEs not only stabilize the long-range ferromagnetic order in 2D and bulk Fe_3GeTe_2 but also enable these materials to have promising applications in high density magnetic data storage. Through electronic structure analysis, we find the strong MAE to originate from the strong SOC introduced by the heavy Te atoms and the coupling with the half-filled $3d$ states on the Fe-II sites. Secondly, all calculated optical spectra are similar due to weak interlayer coupling. The DC-limit of the real part of the magneto-optical conductivity σ_{xy}^1 (i.e., anomalous Hall conductivity) is large and in good agreement with experiments. Also, by derived dipole selection rules, we have assigned the main peaks in the MO spectra to the main optical transitions between the en-

ergy bands in the calculated band structures. Thirdly, we predict large MOKE and MOFE for 2D as well as bulk Fe_3GeTe_2 . In particular, we discover large MO Kerr rotation angle up to -3.7° for TL Fe_3GeTe_2 . MO Kerr rotation angles of -1.3° , 1.89° , and -2.76° for bulk, ML, and BL Fe_3GeTe_2 are found. These values even surpass that of famous MO materials such as 3d transition metal alloy MnBi. Also, Kerr angles of TL and BL Fe_3GeTe_2 are larger than 2D ferromagnetic semiconductors $\text{Cr}_2\text{Ge}_2\text{Te}_6$ and CrI_2 . Finally, large Faraday rotation angles of up to $-156^\circ/\mu\text{m}$ is found for ML Fe_3GeTe_2 . Other Fe_3GeTe_2 structures have Faraday rotation peaks ranging from 80 to $110^\circ/\mu\text{m}$, which is in the same order as that of MnBi

thin films. Our work suggests that few layers and bulk Fe_3GeTe_2 will have promising applications in MO devices.

ACKNOWLEDGMENTS

The authors acknowledge the support from the Ministry of Science and Technology and the National Center for Theoretical Sciences (NCTS) of The R.O.C. The authors are also grateful to the National Center for High-performance Computing (NCHC) for the computing time.

-
- [1] B. Huang, G. Clark, E. Navarro-Moratalla, D. R. Klein, R. Cheng, K. L. Seyler, D. Zhong, E. Schmidgall, M. A. McGuire, D. H. Cobden, W. Yao, D. Xiao, P. Jarillo-Herrero, and X. Xu, Layer-dependent ferromagnetism in a van der Waals crystal down to monolayer limit, *Nature* **546**, 270 (2017).
- [2] C. Gong, L. Li, Z. Li, H. Ji, A. Stern, Y. Xia, T. Cao, W. Bao, C. Wang, Y. Wang, Z. Q. Qiu, R. J. Cava, S. G. Louie, J. Xia, and X. Zhang, Discovery of intrinsic ferromagnetism in two-dimensional van der Waals crystals, *Nature* **546**, 265 (2017).
- [3] Y. Deng, Y. Yu, Y. Song, J. Zhang, N. Z. Wang, Z. Sun, Y. Yi, Y. Z. Wu, S. Wu, J. Zhu, J. Wang, X. H. Chen, and Y. Zhang, Gate-tunable room-temperature ferromagnetism in two-dimensional Fe_3GeTe_2 , *Nature* **563**, 94 (2018).
- [4] N. D. Mermin and H. Wagner, Absence of ferromagnetism or antiferromagnetism in one- or two-dimensional isotropic Heisenberg models, *Phys. Rev. Lett.* **17**, 1133 (1966).
- [5] M. Gibertini, M. Koperski, A. F. Morpurgo, and K. S. Novoselov, Magnetic 2D materials and heterostructures, *Nat. Nanotechnol.* **14**, 408 (2019).
- [6] K. S. Burch, D. Mandrus, and J.G. Park, Magnetism in two-dimensional van der Waals material, *Nature* **563**, 47 (2018).
- [7] H.-J. Deiseroth, K. Aleksandrov, C. Reiner, L. Kienle, and R. K. Kremer, Fe_3GeTe_2 and Ni_3GeTe_2 – Two New Layered Transition-Metal Compounds: Crystal Structures, HRTEM Investigations, and Magnetic and Electrical Properties, *Eur. J. Inorg. Chem.* **2006**, 1561 (2006).
- [8] B. Chen, J.H. Yang, H.D. Wang, M. Imai, H. Ohta, C. Michioka, K. Yoshimura, and M.H. Fang, Magnetic Properties of Layered Itinerant Electron Ferromagnet Fe_3GeTe_2 , *J. Phys. Soc. Jpn.* **82**, 124711 (2013).
- [9] M. Alghamdi, M. Lohmann, J. Li, P. R. Jothi, Q. Shao, M. Aldosary, T. Su, B. P. T. Fokwa, and J. Shi, Highly Efficient Spin-Orbit Torque and Switching of Layered Ferromagnet Fe_3GeTe_2 , *Nano Lett.* **19**, 4400 (2019).
- [10] Y. Wang, C. Xian, J. Wang, B. Liu, L. Ling, L. Zhang, L. Cao, Z. Qu, and Y. Xiong, Anisotropic anomalous Hall effect in triangular itinerant ferromagnet Fe_3GeTe_2 , *Phys. Rev. B* **96**, 134428 (2017).
- [11] K. Kim, J. Seo, E. Lee, K.-T. Ko, B. S. Kim, B. G. Jang, J. M. Ok, J. Lee, Y. J. Jo, W. Kang, J. H. Shim, C. Kim, H. W. Yeom, B. I. Min, B.-J. Yang, and J. S. Kim, Large anomalous Hall current induced by topological nodal lines in a ferromagnetic van der Waals semimetal, *Nat. Mater.* **17**, 794 (2018).
- [12] X. Wang, Z. Li, M. Zhang, T. Hou, J. Zhao, L. Li, A. Rahman, Z. Xu, J. Gong, Z. Chi, R. Dai, Z. Wang, Z. Qiao, and Z. Zhang, Pressure-induced modification of the anomalous Hall effect in layered Fe_3GeTe_2 , *Phys. Rev. B* **100**, 014407 (2019).
- [13] J. Xu, W. A. Phelan, and C.-L. Chien, Large Anomalous Nernst Effect in a van der Waals Ferromagnet Fe_3GeTe_2 , *Nano Lett.* **19**, 8250 (2019).
- [14] C. Fang, C. H. Wan, C. Y. Guo, C. Feng, X. Wang, Y. W. Xing, M. K. Zhao, J. Dong, G. Q. Yu, Y. G. Zhao, and X. F. Hen, Observation of large anomalous Nernst effect in 2D layered materials Fe_3GeTe_2 , *Appl. Phys. Lett.* **115**, 212402 (2019).
- [15] Z. Feil, B. Huang, P. Malinowski, W. Wang, T. Song, J. Sanchez, W. Yao, D. Xiao, X. Zhu, A. F. May, W. Wu, D. H. Cobden, J.-H. Chu, and X. Xu, Two-dimensional itinerant ferromagnetism atomically thin Fe_3GeTe_2 , *Nat. Mat.* **17**, 778 (2018).
- [16] X. Lin and J. Ni, Layer-dependent intrinsic anomalous Hall effect in Fe_3GeTe_2 , *Phys. Rev. B* **100**, 085403 (2019).
- [17] H. L. Zhuang, P. R. C. Kent, and R. G. Hennig, Strong anisotropy and magnetostriction in the two-dimensional Stoner ferromagnet Fe_3GeTe_2 , *Phys. Rev. B* **93**, 134407 (2016).
- [18] Y.-P. Wang, X.-Y. Chen, and M.-Q. Long, Modifications of magnetic anisotropy of Fe_3GeTe_2 by the electric field effect, *Appl. Phys. Lett.* **116**, 092404 (2020).
- [19] S. Y. Park, D. S. Kim, Y. Lin, J. Hwang, Y. Kim, W. Kim, J.-Y. Kim, C. Petrovic, C. Hwang, S.-K. Mo, H.-j. Kim, B.-C. Min, H. C. Koo, J. Chang, C. Jang, J. W. Choi, and H. Ryu, Controlling the Magnetic Anisotropy of the van der Waals Ferromagnet Fe_3GeTe_2 through Hole Doping, *Nano Lett.* **20**, 95, (2020).
- [20] G.-Y. Guo, W. M. Temmerman, and H. Ebert, First-principles determination of the magnetization direction of Fe monolayer in noble metals, *J. Phys.: Condens. Matter* **3**, 8205 (1991).
- [21] J. C. Tung, and G.-Y. Guo, Systematic *ab initio* study of the magnetic and electronic properties of all 3d transition metal linear and zigzag nanowires, *Phys. Rev. B* **76**,

- 094413 (2007).
- [22] Y. Feng, S. Wu, Z.-Z. Zhu, and G.-Y. Guo, Large magneto-optical effects and magnetic anisotropy energy in two-dimensional $\text{Cr}_2\text{Ge}_2\text{Te}_6$, *Phys. Rev. B* **98**, 125416 (2018).
- [23] P. M. Oppeneer, Chapter 1 Magneto-optical Kerr Spectra, pp. 229-422, in *Handbook of Magnetic Materials*, edited by K. H. J. Buschow. Elsevier, Amsterdam, (2001).
- [24] V. Antonov, B. Harmon, and A. Yaresko, *Electronic structure and magneto-optical properties of solids*, Springer Science & Business Media, (2004).
- [25] Y. Yao, L. Kleinman, A. H. MacDonald, J. Sinova, T. Jungwirth, D.-s. Wang, E. Wang, and Q. Niu, First Principles Calculation of Anomalous Hall Conductivity in Ferromagnetic bcc Fe, *Phys. Rev. Lett.* **92**, 0327204 (2004)
- [26] G.-Y. Guo, Y. Yao, Q. Niu, *Ab initio* Calculation of the Intrinsic Spin Hall Effect in Semiconductors, *Phys. Rev. Lett.* **94**, 226601 (2005).
- [27] M. Mansuripur, *The Principles of Magneto-Optical Recording*, (Cambridge University Press, Cambridge, 1995).
- [28] J. P. Castera, in *Magneto-optical Devices*, Vol. 9 of *Encyclopedia of Applied Physics*, edited by G. L. Trigg (Wiley-VCH, New York, 1996), p. 133.
- [29] G.-Y. Guo, H. Ebert, Band-theoretical investigation of the magneto-optical Kerr effect in Fe and Co multilayers, *Phys. Rev. B* **51**, 12633 (1995).
- [30] G.-Y. Guo, H. Ebert, On the origins of the enhanced magneto-optical Kerr effect in ultrathin Fe and Co multilayers, *J. Magn. Magn. Mater.* **156**, 173 (1996).
- [31] V. K. Gudelli, and G.-Y. Guo, Magnetism and magneto-optical effects in bulk and few-layer CrI_3 : a theoretical GGA + U study, *New J. Phys.* **21**, 053012 (2019).
- [32] P. E. Blochl, Projector augmented-wave method, *Phys. Rev. B* **50**, 17953 (1994).
- [33] G. Kresse and J. Hafner, *Ab initio* molecular dynamics for liquid metals, *Phys. Rev. B* **47**, 558 (1993).
- [34] G. Kresse and J. Furthmuller, Efficient interactive schemes for *ab initio* total-energy calculations using a plane-wave basis set, *Phys. Rev. B* **54**, 11169 (1996).
- [35] J. P. Perdew, K. Burke, and M. Ernzerhof, Generalized Gradient Approximation Made Simple, *Phys. Rev. Lett.* **77**, 3865 (1996).
- [36] O. Jepsen and O. K. Anderson, The electronic structure of h.c.p Ytterbium, *Solid State Commun.* **9**, 1763 (1971).
- [37] S. Grimme, Semiempirical GGA-Type Density Functional Constructed with a Long-Range Dispersion Correction, *J. Comput. Chem.* **27**, 1787 (2006).
- [38] C. S. Wang and J. Callaway, Band structure of nickel: Spin-orbit coupling, the Fermi surface, and the optical conductivity, *Phys. Rev. B* **9**, 4897 (1974).
- [39] P. M. Oppeneer, T. Maurer, J. Sticht, and J. Kübler, *An initio* calculated magneto-optical Kerr effect of ferromagnetic metals: Fe and Ni, *Phys. Rev. B* **45**, 10924 (1992).
- [40] W. Feng, G.-Y. Guo, J. Zhou, Y. Yao, and Q. Niu, Large magneto-optical Kerr effect in noncollinear antiferromagnets $\text{Mn}_3 X$ ($X=\text{Rh, Ir, Pt}$), *Phys. Rev. B* **92**, 144426 (2015).
- [41] B. Adolph, J. Furthmuller, and F. Bechstedt, Optical properties of semiconductors using projector-augmented waves, *Phys. Rev. B* **63**, 125108 (2001).
- [42] W. M. Temmerman, P. A. Sterne, G.-Y. Guo, and Z. Szotek, Electronic Structure Calculations of High T_c Materials, *Mol. Simul.* **63**, 153 (1989).
- [43] G.-Y. Guo, K. C. Chu, D.-s. Wang, and C.-g. Duan, Linear and nonlinear optical properties of carbon nanotubes from first-principles calculations, *Phys. Rev. B* **69**, 205416 (2004).
- [44] G.-Y. Guo, and H. Ebert, Theoretical investigation of the orientation dependence of the magneto-optical Kerr effect in Co, *Phys. Rev. B* **50**, 10377(R), 1994.
- [45] Y. Suzuki, T. Katayama, S. Yoshida, K. Tanaka, and K. Sato, New Magneto-Optical Transition in Ultrathin $\text{Fe}(100)$ Films, *Phys. Rev. Lett.* **68**, 3355 (1992).
- [46] N. Sivadas, S. Okamoto, and D. Xiao, Gate-Controllable Magneto-optic Kerr Effect in Layered Collinear Antiferromagnets, *Phys. Rev. Lett.* **117**, 267203 (2016).
- [47] W. Feng, G.-Y. Guo, and Y. Yao, Tunable magneto-optical effects in hole-doped group- IIIA metal-monochalcogenide monolayers, *2D Mater.* **4**, 015017 (2017).
- [48] P. Ravindran, A. Delin, P. James, B. Johansson, J. M. Wills, R. Ahuja, and O. Eriksson, *Phys. Rev. B* **59**, 15680 (1999).
- [49] V. Y. Verchenko, A. A. Tsirlin, A. V. Sobolev, I. A. Presniakov, and A. V. Shevelkov, Ferromagnetic Order, Strong Magnetocrystalline Anisotropy, and Magnetocaloric Effect in the Layered Telluride $\text{Fe}_{3-\delta}\text{GeTe}_2$, *Inorg. Chem.* **54**, 8598 (2015).
- [50] A. F. May, S. Calder, C. Cantoni, H. Cao, and M. A. McGuire, Magnetic structure and phase stability of the van der Waals bonded ferromagnet $\text{Fe}_{3-x}\text{GeTe}_2$, *Phys. Rev. B* **93**, 014411 (2016).
- [51] J.-X. Zhu, M. Janoschek, D. S. Chaves, J. C. Cezar, T. Durakiewicz, F. Ronning, Y. Sassa, M. Mansson, B. L. Scott, N. Wakeham, E. D. Bauer, and J. D. Thompson, Electronic correlation and magnetism in the ferromagnetic metal Fe_3GeTe_2 , *Phys. Rev. B* **93**, 144404 (2016).
- [52] N. Leon-Brito, E. D. Bauer, F. Ronning, J. D. Thompson, and R. Movshovich, Magnetic microstructure and magnetic properties of uniaxial itinerant ferromagnet Fe_3GeTe_2 , *J. Appl. Phys.* **120**, 083903 (2016).
- [53] S. J. Luo, G.-Y. Guo, and A. Laref, Magnetism of 3d-Transition Metal (Fe, Co, and Ni) Nanowires on w-BN (0001), *J. Phys. Chem. C* **113**, 14615 (2009).
- [54] X. Xu, Y. W. Li, S. R. Duan, S. L. Zhang, Y. J. Chen, L. Kang, A. J. Liang, C. Chen, W. Xia, Y. Xu, P. Malinowski, X. D. Xu, J.-H. Chu, G. Li, Y. F. Guo, Z. K. Liu, L. X. Yang, and Y. L. Chen, Signature for non-Stoner ferromagnetism in the van der Waals ferromagnet Fe_3GeTe_2 , *Phys. Rev. B* **101**, 201104(R) (2020).
- [55] G.-Y. Guo, W. M. Temmerman, and H. Ebert, A relativistic spin-polarized band theoretical study of magnetic properties of nickel and iron, *Physica B Condens. Matter* **172**, 61 (1991).
- [56] P. M. Oppeneer, Magneto-optical spectroscopy in the valence-band energy regime: relationship to the magnetocrystalline anisotropy, *J. Magn. Magn. Mater.* **188**, 275 (1998).
- [57] G.H.O Daalderop, P. J. Kelly, and M. F. H. Schuurmans, Magnetocrystalline anisotropy and orbital moments in transition-metal compounds, *Phys. Rev. B* **44**, 21 (1991).
- [58] D.-s. Wang, R. Wu, and A. J. Freeman, First-principles theory of surface magnetocrystalline anisotropy and the diatomic-pair model, *Phys. Rev. B* **47**, 14932 (1993).

- [59] H. Takayama, K.-P. Bohnen, and P. Fulde, Magnetic surface anisotropy of transition metals, *Phys. Rev. B* **14**, 2287 (1976).
- [60] P. G. van Engen, K. H. J. Buschow, R. Jongebreur, and M. Erman, PtMnSb, a material with very high magneto-optical Kerr effect, *Appl. Phys. Lett.* **42**, 202 (1983).
- [61] G. Q. Di, and S. Uchiyama, Optical and magneto-optical properties of MnBi film, *Phys. Rev. B* **53**, 3327 (1996).
- [62] T. Higo, H. Man, D. B. Gopman, L. Wu, T. Koretsune, O. M. J. van 't Erve, Y. P. Kabanov, D. Rees, Y. Li, M.-T. Suzuki, S. Patankar, M. Ikhlas, C. L. Chien, R. Arita, R. D. Shull, J. Orenstein, and S. Nakatsuji, Large magneto-optical Kerr effect and imaging of magnetic octupole domains in an antiferromagnetic metal, *Nat. Photonics* **12**, 73 (2018).
- [63] S. Tomita, T. Kato, S. Tsunashima, S. Iwata, M. Fujii, and S. Hayashi, Magneto-Optical Kerr Effects of Yttrium-Iron Garnet Thin Films Incorporating Gold Nanoparticles, *Phys. Rev. Lett.* **96**, 167402 (2006).
- [64] W.-K. Li, and G.-Y. Guo, A First Principle Study on Magneto-Optical Effects and Magnetism in Ferromagnetic Semiconductors $Y_3Fe_5O_{12}$ and $Bi_3Fe_5O_{12}$, arXiv, 2005.14133 (2020).
- [65] R. Lang, A. Winter, H. Pascher, H. Krenn, X. Liu, and J. K. Furdyna, Polar Kerr effect studies of $Ga_{1-x}Mn_xAs$ epitaxial films, *Phys. Rev. B* **72**, 024430 (2005).
- [66] W.-Y. Tong, S.-J. Gong, X. Wan, C.-G. Duan, Concepts of ferrovalley material and anomalous valley Hall effect, *Nat. Comms* **7**, 13612 (2016).